# Development of A Mission-Tailored Tail-Sitter MAV

Luiz F. T. Fernandez*[1,2], Murat Bronz †[1], Nathalie Bartoli‡[2], and Thierry Lefebvre§[2]

[1]ENAC, Université de Toulouse, F-31400 Toulouse, France
[2]ONERA/DTIS, Université de Toulouse, Toulouse, France

ABSTRACT

Vertical takeoff and landing (VTOL) vehicles are among the most versatile UAVs, appropriate for various missions. Given that there are still open challenges regarding the VTOL design, this paper presents the full development and test cycle of a tail-sitter. IMAV 2022 competition rules are used to define the mission objective and constraints. A multidisciplinary design and optimization strategy is defined with the goal of maximizing competition score considering design, manufacturing, and competition constraints. While still being a work in progress, the resulting vehicle is designed to fly at 18 m/s, for around 14 minutes while carrying 200g of payload and weighting approximately 750g.

## 1 INTRODUCTION

Unmanned aerial vehicles (UAVs) have been object of study of several different research areas in the last decades. One can attribute this fact to two main reasons. From one side, such kind of vehicle can potentially be used for different missions, both civil and military. On the other hand, the technology poses a big variety of challenges to the aerial robotics community, which has primarily emerged from aerospace and robotics engineering fields. This community leverages from the fact that these vehicles can be designed and built with minimal cost, making it very attractive for real world testing and deployment. On the application side, there has been studies to use drones for fire fighting [1, 2], for searching marine debris [3], and even for covid mitigation [4]. Along with several studies regarding perception [5, 6], control is arguably one of the most studied fields within the UAV community [7, 8, 9] just to name a few. As for the design aspect of UAVs and specially micro aerial vehicles (MAVs), fewer studies have been published. Wang et al [10] presented a preliminary design methodology for small tail-sitters that considers weight and power models. Holsten et al. [11] presented the design strategy and wind tunnel test results for a multi-purpose tilt-wing platform. Vogeltanz [12] presented the design and analysis of the mini-UAV tail-sitter named "V-TS", including 2D and 3D high fidelity aerodynamic analysis and flight dynamics modeling. A very extensive review on design and flight control techniques is presented by Ducard and Allenspach [13]. This work tackles both vehicle design and control simultaneously, with the goal to obtain the most suitable vehicle to operate a given mission. In this context, MAV competitions are interesting as they pose well defined missions, suitable for testing and comparing design strategies.

*luiz.tiberio@onera.fr
†murat.bronz@enac.fr
‡nathalie.bartoli@onera.fr
§thierry.lefebvre@onera.fr

Figure 1: Sequential imagery of vertical take-off and transition of the finalized prototype with a close-up picture.

The objective of this paper is to describe the full development cycle of a MAV, shown in Figure 1, providing the readers the possibility to understand our design decisions from the first iteration, how such decisions affected the initial tests, and how such tests affected our design process, in a spiral cycle. We present the initial design strategy, followed by manufacturing technique, and flight testing execution and results. Then another iteration is performed applying the knowledge obtained with initial flights and wind tunnel tests.

In Section 2, we explain the IMAV 2022 competition rules and score calculation. Our design philosophy and optimization strategy is detailed in Section 3. In Section 4, we show our preliminary analysis of the chosen configuration and candidate designs. Section 6 presents the manufacturing techniques and Section 7 details our test campaigns. Section 8 then uses the gathered knowledge to refine the MDO process, with the resulting vehicle, named *Falcon*, being presented in Section 9 along with flight test results. We show our conclusions and perspectives in Section 10.

## 2 COMPETITION RULES AND SCORE ANALYSIS

The IMAV 2022 "Delivery far and fast" competition will be held in the Netherlands. The overall mission objective is to design and operate an MAV capable of carrying a specific amount of payload in a designated outdoor flight field. The

http://www.imavs.org/

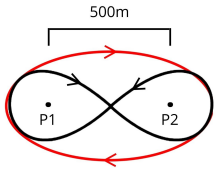


Figure 2: Schematics of competition track and trajectories

score is defined as:

$$score = \frac{N_{laps}(D+1)AP}{W_{vehicle}/W_{max}} \quad (1)$$

Table 1 describes each component of Eq. (1).

| Parameter | Definition |
|---|---|
| $N_{laps}$ | number of laps |
| $D$ | 1 if landed with payload and 0 otherwise |
| $A$ | Autonomy level |
| $P$ | Payload point factor |
| $W_{vehicle}$ | Vehicle weight |
| $W_{max}$ | Maximum allowed weight of 5kg |

Table 1: Score factors

Given that P1 and P2 are obstacles located at $500m$ from each other, a lap can be defined in the following order: visit the line orthogonal to the line P1P2, pass through P1, visit the line orthogonal to the line P1P2 again, and pass through P2. Figure 2 shows a representation of the mission and two compliant trajectories (black and red lines). The autonomy factor ($A$) can assume the values: 1 (remote piloted UAV through video link), 2 (autonomous flight control), and 5 (autonomous mission control). The point factor ($P$) is defined as a function of the payload, as shown in Table 2.

| Payload package mass [$g$] | $P$ (Points factor) |
|---|---|
| 100 | 1 |
| 200 | 2 |
| 500 | 3 |
| 1000 | 4 |

Table 2: Payload and Points factor

Throughout this paper, we will assume that the mission will be fully autonomous ($A = 5$), and no additional constraints for landing will be used to handle the parameter "$D$". The overall mission time is constrained to 30 minutes, including not only the full flight, but also the time expended to put the vehicle in the flight arena and turn on the electronics. So, a maximum flight time of 23 minutes is assumed.

From Eq. (1), we can observe that the mission score is mainly driven by the number of laps ($N_{laps}$) and vehicle weight ($W_{vehicle}$). As the number of laps is mainly a function of flight velocity, increasing this factor might imply in greater propulsion, battery and structural weight, which in turn is reversely proportional to the score. Thus, there is an implicit trade off in the score equation with respect to flight speed and vehicle weight. Such particularity makes the selection of design point more complicated when using traditional design techniques, as too much emphasis could be given to only one aspect of mission score. We used a multidisciplinary optimization (MDO) approach that allowed us not only to better explore the design space and the trade off, but specially to find the optimal design with respect to the score.

(a) FoxTech H-wing (b) Transition Robotics QuadShot

Figure 3: Baseline designs

## 3 DESIGN PHILOSOPHY

The initial hypothesis for this process was that a flying wing tail-sitter with four motors and no aerodynamic control surfaces was the most suitable configuration for this mission. Flying wing MAVs tend to have lower weights, and the use of four motors would allow for vectorized thrust based control, which in turn removes the necessity of control surfaces and additional servos. Figure 3 shows two MAVs used as baseline for our design process, the H-wing by Foxtech [1], and the QuadShot [2] by Transition Robotics.

The employed MDO approach was formulated to maximize the competition score by varying wing planform, angle of attack, and battery mass. Figure 4 shows the extended design structure matrix, as proposed by Lambe and Martins [14], created using WhatsOpt [15]. The optimization process consists of a multidisciplinary analysis (MDA) module and the mission score calculation. The MDA is a non-linear system of equations of three different disciplines: aerodynamics, mission analysis, and weights.

### 3.1 Aerodynamic analysis

OpenAerostruct [16] (OAS) was used for the aerodynamic analysis. It uses a vortex lattice method (VLM) to calculate aerodynamic coefficients. The MH45 airfoil was selected for the first iteration of the analysis. Table 3 shows that the payload dimensions, stipulated by the competition, are representative when considered to general MAV dimensions, so its drag can not be disregarded. Even if a greater payload tends to increase the score when considering the points factor ($P$),

[1] https://www.foxtechfpv.com/
[2] https://transition-robotics.com/pages/projects

http://www.imavs.org/

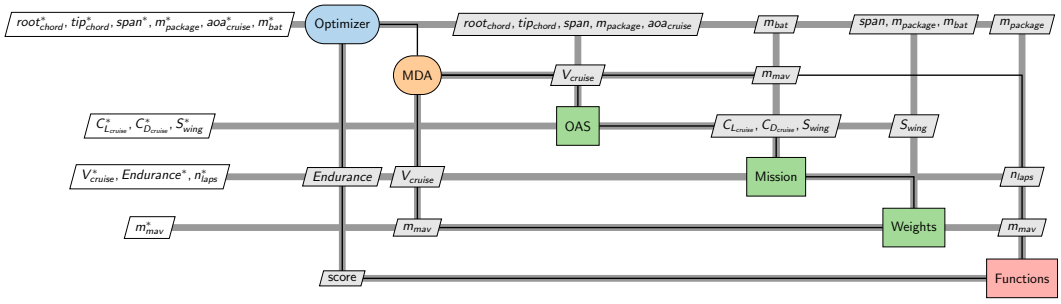


Figure 4: Extended design structure matrix of the tail-sitter process

| Payload mass [$g$] | Dimensions lxbxh [$mm$] |
|---|---|
| 100 | 100x60x40 |
| 200 | 100x80x60 |
| 500 | 150x100x70 |
| 1000 | 145x130x110 |

Table 3: Payload dimensions

this choice would directly lead to greater weights, both structural and battery, and drag. The payload drag coefficient ( $C_{D_{Payload}}$), which is a rectangular body, was fixed to 1.2 according to Carvill [17]. Summarizing, the aerodynamic module calculates the total lift and drag coefficients for a given wing geometry, payload mass, and flight velocity.

## 3.2 Mission analysis and sizing

The mission module calculates flight speed, range, endurance, and number of laps for a given set of aerodynamic coefficients, wing area, MAV total mass, and battery mass. The cruise velocity ($V_{cr}$) is calculated to reinforce that lift is equal to weight in non-accelerated flight as:

$$V_{cr} = \sqrt{\frac{m_{mav} g}{0.5 \rho S C_L}} \tag{2}$$

where $m_{mav}$ is the vehicle mass, $g$ the gravity acceleration, $\rho$ the air density, $S$ the wing reference area, and $C_L$ the lift coefficient in cruise condition. The flight range ($R$) can be obtained for a given battery mass ($m_{bat}$) and vehicle mass as:

$$R = \frac{m_{bat}}{m_{mav} g} B_{SE} \eta \frac{C_L}{C_D} \tag{3}$$

where $C_D$ is the drag coefficient during cruise, the battery specific energy ($B_{SE}$) was assumed to be $140 \frac{Wh}{kg}$ and overall propulsive system efficiency $\eta$ was assumed to be $0.32$. Flight endurance ($E$) is then:

$$E = \frac{R}{V_{cr}}. \tag{4}$$

In order to obtain the number of laps, the lap distance was decomposed into two parts of straight 500m level flight, and two turns. The turn radius was calculated as:

$$T_R = \frac{V_{cr}^2}{g\sqrt{n^2 - 1}} \tag{5}$$

where the load factor ($n$) was fixed in 1.5, which corresponds to an approximately 50°bank angle. The number of laps was then obtained as the integer part of the ratio between flight range and lap distance:

$$N_{laps} = \lfloor \frac{R}{500 + 500 + 2\pi T_R} \rfloor \tag{6}$$

## 3.3 Weights module

The MAV total weight is obtained as a sum of fixed electronics, battery, spar, and structural weight. Table 4 shows the weight breakdown of fixed components.

| Component | Mass [$g$] |
|---|---|
| Autopilot | 12.0 |
| Xbee module | 5.2 |
| Speed controller | 20.7 |
| RC receiver | 7.7 |
| Motor (each) | 17.0 |
| Motor arm (each) | 35.0 |
| GPS module | 50.0 |
| Cables | 30.0 |

Table 4: Fixed weight breakdown

Using previous experience with 3D printed structures from[18], we chose to use this manufacturing technique with carbon tubular spars. We used high and low quality existing printed pieces to obtain an average of the surface weight as a function of its area. The obtained results are shown in Table 5. The wing spar weight was calculated considering 5mm carbon tube. Previous experience shows that instead of using one single spar in the full span, the usage of two spars with 50% span length each provides better rigidity, restricts the rotation motion, and ease component assembly without compromising the wingtip structural integrity or increasing weight.

http://www.imavs.org/

| Structural rigidity | density of area $[g/m^2]$ |
|---|---|
| High | 2485 |
| Low | 941 |
| Average | 1713 |

Table 5: 3D printed structure weight as function of its area

### 3.4 MDO implementation

The MDO loop was implemented using OpenMDAO [19] and all the models were implemented in Python. The non-linear Gauss-Seidel method was selected for solving the MDA and we used IPOPT (Interior Point OPTimizer) from PyOptSparse [20] as the optimizer. Table 6 shows the design variables, objective, and constraints. For the optimization, the mission score is calculated as:

$$\text{score} = N_{laps}\frac{P}{m_{mav}g} \tag{7}$$

| | Function/Variable | Lower | Upper |
|---|---|---|---|
| Maximize | score | | |
| With respect to | Root chord | 0.09 $m$ | 0.4 $m$ |
| | Tip chord | 0.05 $m$ | 0.4 $m$ |
| | Span | 0.3 $m$ | 1.0 $m$ |
| | cruise $\alpha$ | $-10°$ | $10°$ |
| | Payload | 0.1 $kg$ | $1kg$ |
| | Battery mass | 0.01 $kg$ | 1.00 $kg$ |
| Subject to | Endurance | | 23 $min$ |

Table 6: MDO problem formulation

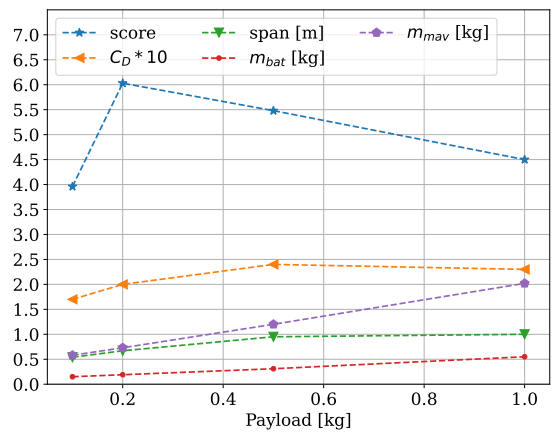


Figure 5: Maximized score, wing span and total drag for the allowed payloads.

| Design variables | Value |
|---|---|
| Root chord | 0.09 $m$ |
| Tip chord | 0.05 $m$ |
| Wing span | 0.66 $m$ |
| Cruise $\alpha$ | $8.73°$ |
| Battery mass | 0.19 $kg$ |
| **Coupling variables** | **Value** |
| Wing area | 0.0467 $m^2$ |
| Cruise speed | 17.7 $m/s$ |
| Cruise $C_L$ | 0.91 |
| Cruise $C_D$ | 0.20 |
| Flight time | 23 $min$ |
| Number of laps | 21 |
| MAV mass | 0.74 $kg$ |

Table 7: Optimal MAV characteristics

## 4 DESIGN ANALYSIS

We started our analysis by evaluating how the competition score is effected by the different allowed payloads, shown in Table 3. For that, the MDO was executed four times, each of them for a fixed payload value. Figure 5 shows the characteristics of the obtained vehicles. It can be noted that choosing the smaller payload possible (100g) would lead to a non-competitive score, while the best values were found for the higher payloads. As it would be expected, the increase in payload mass also leads to bigger wing areas, which in turn increases the drag in cruise. The biggest payload designs are penalized by the drag generated by the bigger fuselage and wing. Figure 5 also shows that the observed difference in drag generates a significant difference in terms of battery and total weight.

This analysis showed that using $200g$ of payload mass for the first design iteration will be beneficial. Table 7 shows the characteristics of the first optimized MAV.

## 5 FLIGHT CONTROL SYSTEM

We used Paparazzi[3] system [21], which allows for the automation of flight tasks up to complete autonomous flight for a designated route. The implemented INDI control law, successfully applied to tail-sitter in [9], was employed. The gains were estimated based on previous experience with tail-sitter and then refined after flight experiments. For the competition, the flight trajectory can be defined through Paparazzi's flight plan, and all the flight phases can to be fulfilled autonomously including safety measures, such as low-battery and GPS-lost mitigation maneuvers.

## 6 MANUFACTURING

One of the main objectives of this work is to showcase the iterative refining of the MDO process of the design for IMAV-2022's mission profile. Therefore, an agile manufacturing technique is chosen as proposed in Bronz et al. [18]

[3] https://wiki.paparazziuav.org/wiki/Main_Page

http://www.imavs.org/

http://www.imavs.org/

using 3D printing. Such strategy allows for rapid manufacturing of different parts, which in turn enables faster design iterations.

## 7 FLIGHT TESTS

An iterative flight test procedure was followed, where the complexity of the mission increases according to the outcome of each test.

### 7.1 Hovering tests

The first hover test was conducted using only the main body of the vehicle inside ENAC's flight arena, as shown in Figure 6, while waiting for the manufacturing of the wing pairs. The gathered data were used to fine-tune the efficiency matrix of the INDI [9] controller for hover phase and proved that the vehicle is capable of stable hover with the designated payload capacity. The wings were then assembled for the second hover test.

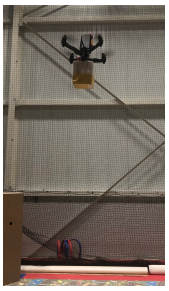

Figure 6: Hover test

### 7.2 Outdoor flight tests

After successfully performing the hovering test, the vehicle was tested in an outdoor flight field. Throughout the first day of tests, six successful non-autonomous flights were performed, with increasing level of difficulty starting from simple hover to the full flights with takeoff, cruise, and landing. Figure 7 shows the trajectory of the third flight, whose data will be shown from now on. After this approximately

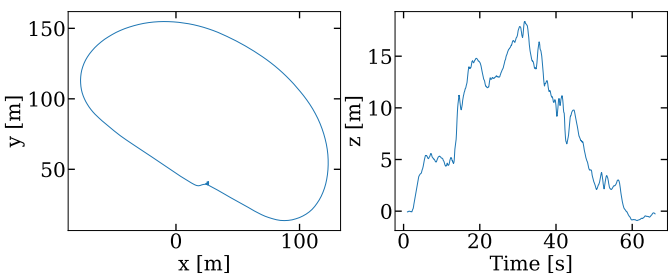


Figure 7: Experimental flight trajectory in XY plane and altitude.

one minute flight, the motors were overheated, indicating that an overload could be occurring. By analyzing Figure 8, that shows power consumption throughout the flight, it is indeed possible to note that even during cruise the motors are heavily loaded and no significant difference was observed between hover and cruise, which should not be the case for a winged vehicle. With such high values of power, the vehicle would

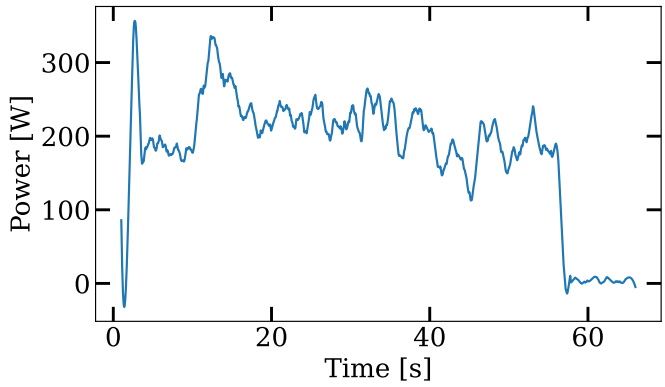


Figure 8: Experimental flight power consumption

not be able to perform the proposed 23 minutes mission. So it became necessary to investigate the source of such power consumption, with two main candidates:

- The set motors-propellers could be inadequate in terms of allowing for high range cruise and control authority. The only possibly suitable propellers available at that moment were the GS 5.0x4.5, but smaller diameters could increase cruise efficiency.
- The predicted drag polar could be overly optimistic for both lift and drag.

#### 7.2.1 Propulsion system testing and autonomous flights

In order to compare different sizes of propellers and its impact on the performance, a new batch of outdoor tests was prepared and executed. We performed two fully autonomous flights, with the same trajectory and setpoints of 18 $m/s$ and 30 $m$ for cruise velocity and altitude, respectively. The only difference between flight two and flight three were the propellers, the already discussed GS 5.0x4.5 (flight two) and the smaller GS 4.0x4.5 (flight three) were used. The outcome in terms of trajectory was quite similar, as presented in Figure 9, which allows for a fair comparison between propellers. Figure 10 shows that flight number three, with the smaller propeller, shows indeed a slightly smaller current and presents a higher voltage at the end of the flight. However, such improvement would still not make the 23 minutes flight possible as the power demand remains high, as shown in Figure 11. As a result, the autonomous flight capability was validated, and the hypothesis that a bigger propeller was causing an increase in the energy consumption was confirmed, even though the influence is small. Nevertheless, we opted for including

http://www.imavs.org/

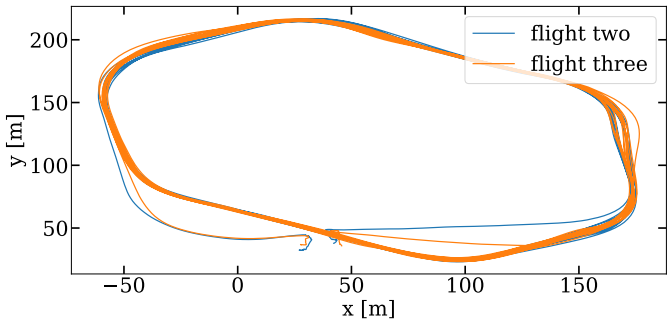


Figure 9: Autonomous flight two and three trajectories in XY plane

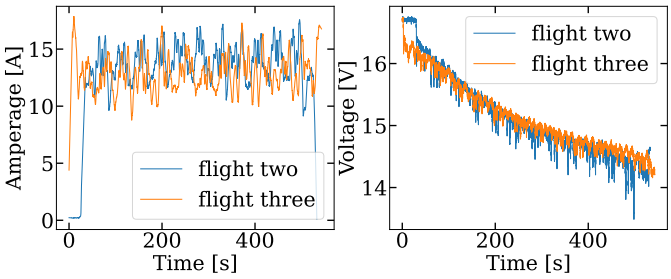


Figure 10: Autonomous flight two and three current and voltage

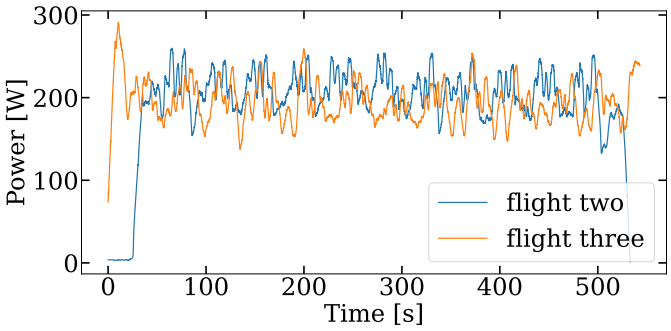


Figure 11: Autonomous flight two and three power consumption

propeller analysis in the second iteration of the MDO, as discussed later.

## 7.3 Drag evaluation

In order to validate both lift and drag predictions, the vehicle was tested in a wind tunnel. The experiments were performed inside ENAC's (French Civil Aviation University) flight arena in Toulouse, France. The wind tunnel, designed by WindShape [4] has a $1.5\,m$ by $0.75\,m$ open test section and is used both for research and educational purposes. Force and moments were measured with a six-axis ATI Mini-40 sensor [5] calibrated with SI-40-2, with maximum force range of 40N for $F_{xy}$, 120N for $F_z$ and $1/100\,N$ resolution for xy and $1/50\,N$ resolution for z. The moment range is 2Nm for $M_{xyz}$ with a $1/4000\,Nm$ resolution. The vehicle was tested in a single airspeed representative velocity of 19.5 $m/s$ and for four equally spaced angles of attack between 0°and 22.5°. Figure 12 shows the vehicle in front of the test section.

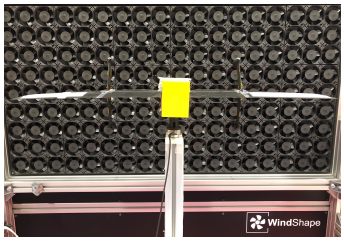


Figure 12: Vehicle attached to the force and moment balance in front of WindShape.

In order to understand the contributions of each drag source in cruise flight, the vehicle was tested in different configurations: full vehicle, without wings, without mounting arms, without wings and mounting arms, and without payload. The result of this test is shown in Figure 13. The core drag is mainly driven by the battery and autopilot module, which are fixed. The test showed that the mounting arms were the most dominant component with respect to drag generation, responsible for almost half of the total drag. Hence we decided to evaluate a different configuration for this component, in order to reduce such behavior. Another vehicle was printed with the arms in "H" configuration, as shown in Figure 14. But little difference was observed. "X" configuration arms led to slightly higher $C_L$ for small angles of attack, as shown in Figure 15. So we chose to maintain the "X" geometry mainly because of its simplicity and light weight.

The outcome of the wind tunnel tests was then used to refine the second version of the aerodynamic module of the MDO.

## 7.4 Lift evaluation

By analyzing Figure 15, it is also possible to observe that the predicted $C_L$ of 0.91 for an angle of attack of about 9°,

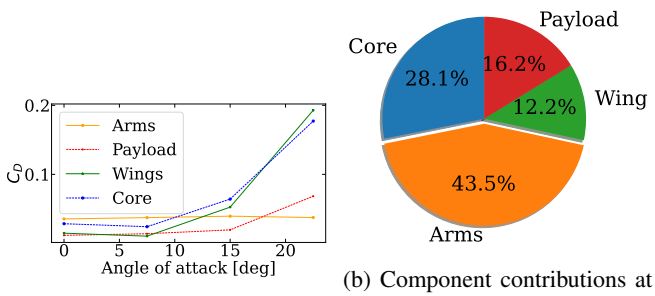


(a) Drag with respect to α (b) Component contributions at $\alpha$ of 7.5°

Figure 13: Wind tunnel test outcome

[4] https://windshape.com/technology/
[5] https://www.ati-ia.com/products/ft/ft_models.aspx?id=mini40

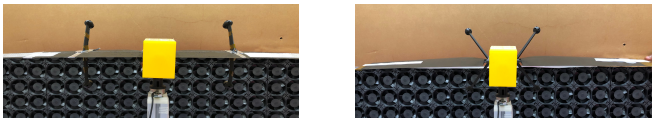

(a) Mounting arms in "H" (b) Mounting arms in "X"

Figure 14: Test setup for arm configuration study. Half of the WindShape test section was covered to ease the visualisation.

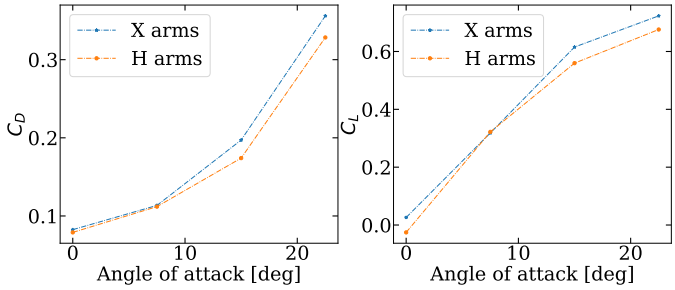


Figure 15: Comparison of arm configuration

shown in Table 7 was unfeasible. The actual value is less than half of the predicted value. The consequence for that can be seen in Figure 16, showing that pitch angle for both flight two and flight three were higher than 20°during the whole cruise flight, a flight regime that can be considered to be stalled, even if the real angle of attack is not known. As the wing lift was overestimated, the autopilot had to increase the pitch angle to ensure that the required force to compensate the weight was generated, but at such high pitch angles, only the motors were generating lifting force, while the stalled wings were mostly contributing to the drag, penalizing flight efficiency.

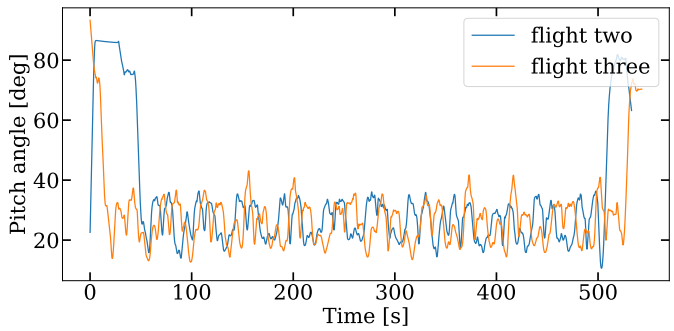


Figure 16: Pitch angle for flight two and three.

This is believed to have caused the lack of performance observed during the initial flights. The lack of lift was most likely generated by non considered interference effects and 3D printing inaccuracies, while the process was still being refined. In order to handle that for the second iteration of the MDO, the lift output from OpenAerostruct was tuned to match the observed data, as it will be shown.

## 8 MDO PROCESS REFINEMENT

The results obtained in the first batch of flight tests have shown that the initial MDO formulation was possibly over-simplified. The assumption made in Eq. (2) was that, in cruise, thrust is equal to weight, and that the required thrust would be available throughout the entire flight. There were no corrections for lift and drag prediction, which led to a small wing area, incapable of maintaining sustained level flight at low angles of attack and culminating in poor performance. In order to refine our methodology and mitigate these effects, we have added new constraints for hover flight and turning maneuver and refined the aerodynamic module.

### 8.1 Propulsion refinement

#### 8.1.1 Thrust calculation

In order to obtain thrust ($T$) in both hover and cruise flight conditions, we employed CCBlade [6], a blade element momentum method formulation that is specially suited for gradient based optimization presented by Ning [22]. As CCBlade is implemented in Julia, we developed a wrapper to call it from our Python environment. With CCBlade, the thrust generated is calculated as a function of airspeed, propeller geometry and rpm. We employed Xfoil [23] to account for the correct propeller airfoil polar in the optimization loop.

#### 8.1.2 Hover analysis

In order to account for the hover capability, a new constraint was implemented:

$$\frac{a_z}{m} = 0.9T - m_{mav}g \geq 0 \tag{8}$$

The acceleration in the $z$ axis ($a_z$), calculated as the difference between the thrust ($T$) generated by the four propellers and MAV weight ($m_{mav}g$) is constrained to be greater than 0, in order to ensure hover capability. We added a safety margin of 10% to account for eventually necessary attitude corrections that would require thrust in other directions than $z$.

#### 8.1.3 Turn maneuver analysis

Similarly, a constraint to ensure that in the forward flight ($x$) axis there is enough thrust to generate positive or zero acceleration ($a_x$), was added:

$$\frac{a_x}{m} = T - D \geq 0 \quad at \quad V_{turn} \tag{9}$$

where the both lift ($C_{L_{turn}}$) and drag ($C_{D_{turn}}$) were also obtained using OpenAeroStruct. Thrust ($T$) is now assumed as the sum of the thrust from all the motors operating with a safety margin of 15%. Velocity ($V_{turn}$) can be calculated as

$$V_{turn} = \sqrt{\frac{m_{mav}gn}{0.5\rho S C_{L_{turn}}}} \tag{10}$$

[6] https://github.com/byuflowlab/CCBlade.jl

http://www.imavs.org/

http://www.imavs.org/

where the load factor $n$ accounts for the decrease in lift generated by the bank angle.

Considering this more detailed problem formulation, we were also able to refine range and endurance calculation. The turning radius from Eq. (5) is now calculated as a function of $V_{turn}$ :

$$T_R = \frac{V_{turn}^2}{g\sqrt{n^2-1}}. \tag{11}$$

Such new formulation allowed to split each lap into two different flight conditions: 1000 $m$ cruise flight and a bank flight with a length of $2\pi T_R$ $m$. With that, relations for average airspeed, lift and drag coefficient were adopted:

$$V_{avg} = V_{cruise}(1 - \frac{2\pi T_R}{1000}) + V_{turn}\frac{2\pi T_R}{1000} \tag{12}$$

$$C_{L_{avg}} = C_{L_{cruise}}(1 - \frac{2\pi T_R}{1000}) + C_{L_{turn}}\frac{2\pi T_R}{1000} \tag{13}$$

$$C_{D_{avg}} = C_{D_{cruise}}(1 - \frac{2\pi T_R}{1000}) + C_{D_{turn}}\frac{2\pi T_R}{1000} \tag{14}$$

which in turn allow us to refine the range from Eq. (3) and endurance from Eq.( 4):

$$R = \frac{m_{bat}}{m_{mav}g}B_{SE}\eta\frac{C_{L_{avg}}}{C_{D_{avg}}} \qquad E = \frac{R}{V_{avg}} \tag{15}$$

#### 8.1.4 Aerodynamic calculation refinement

In order to enhance the drag prediction in the MDO process, we used the wind tunnel test results at representative velocity to refine the drag calculation. As shown in Figure 13a, both payload and motor arm drag can be assumed as constant at such speed for angles of attack lower than 15°. The core drag was approximated with a second order polynomial function, varying according to the angle of attack. The wing drag, calculated from OpenAeroStruct, was kept without changes. The total drag was then calculated as:

$$C_D = C_{D_{OAS}} + C_{D_{core}}(\alpha) + C_{D_{constant}} \tag{16}$$

where

$$C_{D_{constant}} = C_{D_{arms}} + C_{D_{Payload}} \tag{17}$$

For the lift, two changes were made: The predicted lift coefficient for alpha zero ($C_{L0}$) was updated from 0.2 (first MDO iteration) to zero, and a correction of 0.7 was also applied to the output of the OpenAeroStruct. These changes were made with the objective of fitting the predicted lift to the observed one.

#### 8.1.5 Weights module refinement

The weight prediction of the components was also updated considering the information gathered with the first vehicle, as shown in Table 8.

| Component | Mass |
|---|---|
| Motors and arms | 104 $[g]$ |
| Cables | 20.0 $[g]$ |
| Wing density of area | 1360 $[g/m^2]$ |

Table 8: Fixed weight breakdown

### 8.2 Refined MDO formulation

Table 9 shows the new configuration of the MDO problem, with the added design variable and constraints. The design space for the second iteration had to be reduced in order to comply with the manufacturing technique limitation, as problems occurred when printing larger wing spans and smaller tip chords. As the wind tunnel campaign was fully conducted considering the initially defined payload of 0.2 $kg$, this value was fixed in order to ensure precise drag prediction and avoid extrapolations with untested payloads. Even if the analysis presented in Section 4 could have been refined considering the new data, we considered that the trends observed with the first MDO problem were still valid.

| | Function/Variable | Lower | Upper |
|---|---|---|---|
| Maximize | score | | |
| With respect to | Root chord | 0.125 $m$ | 0.2 $m$ |
| | Tip chord | 0.095 $m$ | 0.2 $m$ |
| | Span | 0.3 $m$ | 0.7 $m$ |
| | Cruise α | 1° | 10° |
| | Turn α | 1° | 8° |
| | Battery mass | 0.1 $kg$ | 0.2 $kg$ |
| Subject to | Endurance | | 23 $min$ |
| | $a_x$ | 0 | |
| | $a_x$ | 0 | |

Table 9: MDO problem formulation

For this execution we used the super efficient global optimization coupled with mixture of experts (SEGOMOE) [24], a surrogate-based gradient-free optimizer that can handle expensive and multimodal cases, in order to avoid converging to a local optima.

## 9 OPTIMIZED VEHICLE AND FLIGHT TEST

Table 10 shows the characteristics of the second iteration of the vehicle.

The optimal geometry was then manufactured and flight tested. The vehicle weight was 753 g, 13 g higher than the predicted with the MDO. Due to problems with the guidance module, the flight with the new geometry was not autonomous, what entangles the discussion on flight efficiency. Nevertheless, the flight trajectory was uniform, as shown in Figure 17.

The pitch angle, shown in Figure 18, was smaller and mostly below stall region, which in turn allowed for the de-

| Design variables | Value |
|---|---|
| Root chord | 0.12 $m$ |
| Tip chord | 0.095 $m$ |
| Wing span | 0.7 $m$ |
| Cruise α | 10° |
| Turn α | 8° |
| Battery mass | 0.2 $kg$ |
| **Coupling variables** | **Value** |
| Wing area | 0.075 $m^2$ |
| Cruise speed | 18.0 $m/s$ |
| Cruise $C_L$ | 0.54 |
| Cruise $C_D$ | 0.12 |
| Flight time | 14.6$min$ |
| Number of laps | 13 |
| MAV mass | 0.74 $kg$ |

Table 10: Optimal MAV characteristics at the end of new MDO iteration

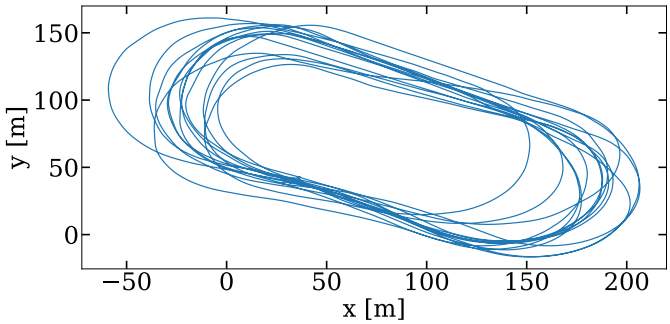


Figure 17: 4th flight XY trajectory.

sired reduction in power consumption, shown in Figure 19.

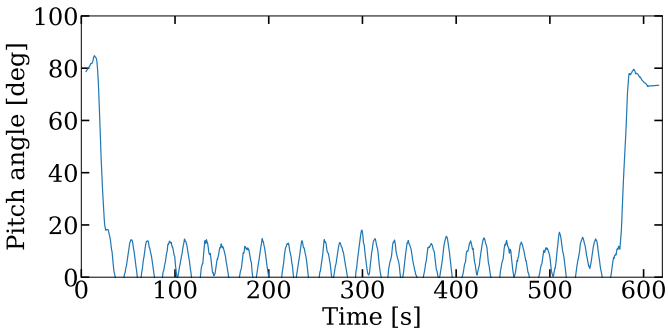


Figure 18: Pitch angle variation during the 4th flight.

During this approximately 10 minutes of flight with longer than usual hover phases, conducted to re-identify the vehicle and refine the INDI controller coefficients, the energy consumed was roughly 19.4$Wh$, using a 4s LiPo battery with 26.9$Wh$ nominal capacity. Considering the flight data, it is estimated that, with the same battery and assuming a complete run consuming around 23$Wh$ to ensure a safety

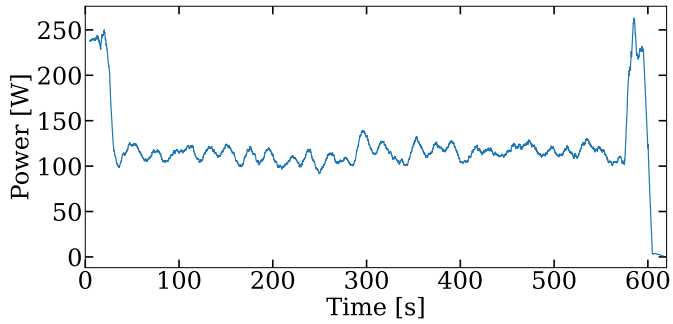


Figure 19: Power consumption during the 4th flight

margin, the predicted flight duration of 14 minutes can be achieved, specially taking into account the benefits from the autonomous flight and a smaller hover phase, which is the most energy consuming portion of the flight.

## 10 CONCLUSION

In this paper we presented a full design and flight testing cycle of an MAV. The vehicle was designed to comply with the IMAV 2022 competition rules, an interesting benchmark for evaluating a design methodology. A multidisciplinary design and optimization approach was selected. The first MDO was a combination of three disciplines: aerodynamics, weights, and mission analysis, and it led to a smaller design, which was built and flight tested. Driven by the necessity of reducing power consumption observed in the first flight test, we conducted wind tunnel tests to identify the main sources of drag and refined the MDO process by adding an improved lift and drag prediction module, created with the results of the experiments, and CCBlade for thrust analysis in both hover and turn maneuver conditions. The design obtained after the second iteration of the MDO presented a more accurate lift prediction, in line with the expectation, which in turn resulted in lower energy consumption during test flights. For future work and the IMAV competition, studies addressing core and payload drag reduction will be conducted, "Li-Ion" batteries will be considered, as existing batteries with 37$Wh$ nominal capacity could allow even longer flights, and the manufacturing process will be refined with the objective of allowing for higher wing spans and, as a result, more design freedom. Additionally, the outcome of autonomous and competition flights are intended to be published in a journal version of this work.

## ACKNOWLEDGMENTS

This work is part of the activities of ONERA - ISAE - ENAC joint research group.

## REFERENCES

[1] Elena Ausonio, Patrizia Bagnerini, and Marco Ghio. Drone swarms in fire suppression activities: A conceptual framework. *Drones*, 5(1), 2021.

http://www.imavs.org/

http://www.imavs.org/

[2] Moulay A. Akhloufi, Andy Couturier, and Nicolás A. Castro. Unmanned aerial vehicles for wildland fires: Sensing, perception, cooperation and assistance. *Drones*, 5(1), 2021.

[3] Yuri Taddia, Corinne Corbau, Joana Buoninsegni, Umberto Simeoni, and Alberto Pellegrinelli. Uav approach for detecting plastic marine debris on the beach: A case study in the po river delta (italy). *Drones*, 5(4), 2021.

[4] Ágoston Restás. Drone applications fighting covid-19 pandemic;towards good practices. *Drones*, 6(1), 2022.

[5] Zichao Zhang and Davide Scaramuzza. Perception-aware receding horizon navigation for mavs. In *2018 IEEE International Conference on Robotics and Automation (ICRA)*, page 2534–2541. IEEE Press, 2018.

[6] Kirk Y.W. Scheper and Guido C.H.E. de Croon. Evolution of robust high speed optical-flow-based landing for autonomous mavs. *Robotics and Autonomous Systems*, 124:103380, 2020.

[7] Robin Ritz and Raffaello D'Andrea. A global controller for flying wing tailsitter vehicles. In *2017 IEEE International Conference on Robotics and Automation (ICRA)*, pages 2731–2738, 2017.

[8] Philipp Hartmann, Carsten Meyer, and Dieter Moormann. Unified velocity control and flight state transition of unmanned tilt-wing aircraft. *Journal of Guidance, Control, and Dynamics*, 40(6):1348–1359, 2017.

[9] Ewoud J. J. Smeur, Murat Bronz, and Guido C. H. E. de Croon. Incremental control and guidance of hybrid aircraft applied to a tailsitter unmanned air vehicle. *Journal of Guidance, Control, and Dynamics*, 43(2):274–287, 2020.

[10] Bo Wang, Zhongxi Hou, Zhaowei Liu, Qingyang Chen, and Xiongfeng Zhu. Preliminary design of a small unmanned battery powered tailsitter. *International Journal of Aerospace Engineering*, 2016:3570581, May 2016.

[11] J. Holsten, T. Ostermann, and D. Moormann. Design and wind tunnel tests of a tiltwing uav. *CEAS Aeronautical Journal*, 2(1):69–79, Dec 2011.

[12] Tomáš Vogeltanz. Conceptual design and control of twin-propeller tail-sitter mini-uav. *CEAS Aeronautical Journal*, 10(3):937–954, Sep 2019.

[13] Guillaume J.J. Ducard and Mike Allenspach. Review of designs and flight control techniques of hybrid and convertible vtol uavs. *Aerospace Science and Technology*, 118:107035, 2021.

[14] Andrew B. Lambe and Joaquim R. R. A. Martins. Extensions to the design structure matrix for the description of multidisciplinary design, analysis, and optimization processes. *Structural and Multidisciplinary Optimization*, 46:273–284, 2012.

[15] Rémi Lafage, Sebastien Defoort, and Thierry Lefebvre. Whatsopt: a web application for multidisciplinary design analysis and optimization. In *AIAA Aviation 2019 Forum*, page 2990, 2019.

[16] John P. Jasa, John T. Hwang, and Joaquim R. R. A. Martins. Open-source coupled aerostructural optimization using Python. *Structural and Multidisciplinary Optimization*, 57(4):1815–1827, April 2018.

[17] J. Carvill. 4 - fluid mechanics. In J. Carvill, editor, *Mechanical Engineer's Data Handbook*, pages 146–171. Butterworth-Heinemann, Oxford, 1993.

[18] Murat Bronz, Jacson Barth, Ezra Tal, Federico Favalli, and Sertac Karaman. Mission-oriented additive manufacturing of modular mini-uavs. In *AIAA Scitech 2020 Forum*, 2020.

[19] Justin S. Gray, John T. Hwang, Joaquim R. R. A. Martins, Kenneth T. Moore, and Bret A. Naylor. OpenMDAO: An open-source framework for multidisciplinary design, analysis, and optimization. *Structural and Multidisciplinary Optimization*, 59(4):1075–1104, April 2019.

[20] Neil Wu, Gaetan Kenway, Charles A. Mader, John Jasa, and Joaquim R. R. A. Martins. pyoptsparse: A python framework for large-scale constrained nonlinear optimization of sparse systems. *Journal of Open Source Software*, 5(54):2564, 2020.

[21] Pascal Brisset, Antoine Drouin, Michel Gorraz, Pierre-Selim Huard, and Jeremy Tyler. The paparazzi solution. In *IMAV 2006*, 10 2006.

[22] Andrew Ning. Using blade element momentum methods with gradient-based design optimization. *Structural and Multidisciplinary Optimization*, 64(2):991–1014, August 2021.

[23] Mark Drela. Xfoil: An analysis and design system for low reynolds number airfoils. In Thomas J. Mueller, editor, *Low Reynolds Number Aerodynamics*, pages 1–12, Berlin, Heidelberg, 1989. Springer Berlin Heidelberg.

[24] N. Bartoli, T. Lefebvre, S. Dubreuil, R. Olivanti, R. Priem, N. Bons, Joaquim R. R. A. Martins, and J. Morlier. Adaptive modeling strategy for constrained global optimization with application to aerodynamic wing design. *Aerospace Science and Technology*, 90:85–102, July 2019.